A theoretical and experimental study of ac electrothermal flows

S Loire, P Kauffmann[1], I Mezić and C D Meinhart

Department of Mechanical Engineering, University of California, Santa Barbara, Santa Barbara, CA, 93106-5070, USA

E-mail: sloire@engr.ucsb.edu

Abstract
Electrokinetic flows lead to promising utilization for mixing, concentration, pumping and have applications from basic studies of convective flows to fully integrated lab on chip developments. Despite these wide applications, electrothermal flow models have been scarcely studied. We find that the model widely used by the microfluidic community does not fit correctly the measured ac electrothermal fluid flows at higher voltages (10 V_{pp} and above). We thus analyse both theoretically and experimentally the importance of electrothermal coupling and the buoyancy effect. Numerical simulations are compared with micro-particle image velocimetry measurements of the vortices. Our enhanced model successfully matches our measurements over a wide range of conductivities and voltages.

(Some figures may appear in colour only in the online journal)

1. Introduction

Driving fluid flows by ac electrokinetics is a useful method to produce three-dimensional convective flows and study their mixing properties. Application of voltage to embedded electrodes can produce a wide range of mixing protocols. Particle-image velocimetry provides for quantitative visualization from an Eulerian frame of such flows, which leads to understanding of Lagrangian structures that govern mixing. Various phenomena produced by ac electrokinetic forcing—where the interaction between electric fields and polarizable and/or conductive solution generates flows—have been characterized, such as ac electro-osmosis (ACEO) and ac electrothermal (ACET) effects [1]. In addition, thermal effects produce buoyancy forces in the fluid. For most electrode and channel designs, these flows appear in the form of vortices used for mixing or pumping [2–4]. ACET involves electric, thermal and fluidic phenomena simultaneously. More than 10 years ago, based on small perturbation theory, Ramos *et al* suggested an elegant ACET model, which has been widely accepted by the community [5]. Recently, Sin *et al* pointed out some differences between this model and their measurement at high conductivities [6]. We propose an extension of the model [5] that accounts for these discrepancies. We first demonstrate

that for high temperature elevation, electrothermal coupling cannot be neglected. Then, we show that the buoyancy force effect has to be taken into account in the case of our mesoscale device. To evaluate the present model, we perform micro-particle-image velocimetry (μPIV) measurements. Numerical simulations of our enhanced model (18) successfully match quantitatively our experimental measurements for a wide range of conductivities and voltages.

2. Background theory

A charged body in an electric field tends to move along the electric field lines and impart momentum to the surrounding fluid. Electrothermal flows are due to the interaction of an electric field with non-uniform permittivity and conductivity. In such a system, a local free charge distribution must be present if Gauss's law and charge conservation are to be satisfied simultaneously:

$$\begin{cases} \boldsymbol{\nabla} \times \boldsymbol{E} = 0, \\ \boldsymbol{\nabla} \cdot (\varepsilon_{\mathrm{m}} \boldsymbol{E}) = \rho_{\mathrm{e}}, & \text{Gauss's law,} \\ \boldsymbol{\nabla} \cdot (\sigma_{\mathrm{m}} \boldsymbol{E} + \rho_{\mathrm{e}} \boldsymbol{u}) + \dfrac{\partial \rho_{\mathrm{e}}}{\partial t} = 0, & \text{charge conservation,} \end{cases}$$

(1)

where σ_{m} is the solution conductivity, ε_{m} the solution permittivity, $\boldsymbol{u}$ the fluid velocity, ρ_{e} the local charge density and $\boldsymbol{E}$ the electric field.

---

[1] This author contributed equally to this work as the first author.

Local charge density, both free and bound, responds to the applied electric field, resulting in a non-zero volume force on the fluid. The electrostatic body force density acting on molecules of an aqueous (incompressible) solution in the presence of an electric field consists in two terms: Coulombian and dielectrophoretic force [7]:

$$\boldsymbol{F}_{ET} = \rho_e \boldsymbol{E} - \frac{1}{2}|\boldsymbol{E}|^2 \vec{\nabla} \varepsilon_m. \tag{2}$$

The convection term $\rho_e \boldsymbol{u}$ in (1) can be ignored since the electric Reynolds number $Re_{el} = \frac{\varepsilon_m u_0}{\sigma_m L} \ll 1$ (u_0 and L are the characteristic velocity and length). Moreover, as the permittivity and conductivity of aqueous solutions depend on temperature, T, the electrical equations become:

$$\begin{cases} \boldsymbol{\nabla} \times \boldsymbol{E} = 0, \\ \varepsilon_m(T)\boldsymbol{\nabla} \cdot \boldsymbol{E} + \boldsymbol{E} \cdot \boldsymbol{\nabla} \varepsilon_m(T) = \rho_e, \\ \sigma_m(T)\boldsymbol{\nabla} \cdot \boldsymbol{E} + \boldsymbol{E} \cdot \boldsymbol{\nabla} \sigma_m(T) + \frac{\partial \rho_e}{\partial t} = 0. \end{cases} \tag{3}$$

Joule heating induces conductivity and permittivity inhomogeneities in the solution. The temperature distribution is given by the Joule heating equation:

$$\rho_m(T)c_p(T)\left(\frac{\partial T}{\partial t} + (\boldsymbol{u} \cdot \nabla)T\right)$$
$$= \boldsymbol{\nabla} \cdot (k_m(T)\boldsymbol{\nabla}T) + \sigma_m(T)|\boldsymbol{E}|^2, \tag{4}$$

where k_m is the fluid heat conductivity, ρ_m the fluid density and c_p the fluid heat capacitance and $\sigma_m|\boldsymbol{E}|^2$ is the Joule heating term. For small thermal Peclet number, $Pe_T = \frac{\rho_m c_p u_0 L}{k} \ll 1$, thermal convection can be neglected in (4). Note that for typical length $L = 250\,\mu$m, $Pe_T \approx 1$ for $u_0 = 500\,\mu$m s^{-1}.

The fluid velocity, in such systems typically with low Reynolds number ($Re = \frac{\rho_m u_0 L}{\mu_m} \ll 1$) is given by Stokes equation:

$$\rho_m(T)\frac{\partial \boldsymbol{u}}{\partial t} = -\boldsymbol{\nabla}P + \boldsymbol{\nabla} \cdot (\mu_m(T)(\boldsymbol{\nabla}\boldsymbol{u} + (\boldsymbol{\nabla}\boldsymbol{u})^T) + \boldsymbol{F},$$
$$\boldsymbol{\nabla} \cdot \boldsymbol{u} = 0, \tag{5}$$

where μ_m is the fluid viscosity and P is the fluid pressure. The body force $\boldsymbol{F}$ is composed of the electrostatic body force $\boldsymbol{F}_{ET}$ defined in (2) and the buoyancy force $\boldsymbol{F}_b = \rho_m(T_0)(T - T_0)\beta \boldsymbol{g}$, where $\beta = 10^{-3}\,^\circ$C^{-1} is the coefficient of thermal expansion and $\boldsymbol{g} = -9.8\,$m s$^{-2}\boldsymbol{z}$ is the acceleration of gravity, T_0 is the temperature of reference.

This system of equations was elegantly simplified by Ramos *et al* [5], using a small temperature gradient approximation, to permit easier simulations and understanding of the velocity dependence on the applied voltage. In the approximation of small temperature gradients, the changes in fluid properties are assumed to be small. The electric field is calculated as the sum of the isothermal solution and a small perturbation:

$$\boldsymbol{E} = \boldsymbol{E}_0 + \boldsymbol{E}_1,$$
$$\text{with } \boldsymbol{E}_1 \ll \boldsymbol{E}_0, \text{ and } \boldsymbol{\nabla} \cdot \boldsymbol{E}_0 = 0. \tag{6}$$

Considering an ac signal with angular frequencies ω, the body force is given by evaluating ρ_e using an expression of $\boldsymbol{\nabla} \cdot \boldsymbol{E}_1$ in terms of $\boldsymbol{E}_0$ in the time-averaged ACET force (2):

$$\langle \boldsymbol{F}_{ET}\rangle = \frac{\varepsilon_m(T_0)}{2}\Bigg[(c_\varepsilon - c_\sigma)\frac{\boldsymbol{\nabla}T \cdot \boldsymbol{E}_0}{1 + (\omega\tau)^2}\boldsymbol{E}_0$$
$$- \frac{1}{2}c_\varepsilon \boldsymbol{\nabla}T|\boldsymbol{E}_0|^2\Bigg]. \tag{7}$$

For aqueous solutions, a linear approximation of the temperature dependence of the electrical conductivity and permittivity is adequate, $\sigma_m(T) = \sigma_m(T_0)(1 + c_\sigma(T - T_0))$ and $\varepsilon_m(T) = \varepsilon_m(T_0)(1 + c_\varepsilon(T - T_0))$ where $c_\sigma = \frac{1}{\sigma(T_0)}(\frac{\partial\sigma}{\partial T})|_{T_0} \approx 0.02\,^\circ$C^{-1} and $c_\varepsilon = \frac{1}{\varepsilon(T_0)}(\frac{\partial\varepsilon}{\partial T})|_{T_0} \approx -0.004\,^\circ$C^{-1} [8], with T_0 being a temperature of reference. The time $\tau = \varepsilon(T_0)/\sigma(T_0)$ represents the charge relaxation time. The ACET flow is hence estimated by solving the following set of equations:

$$\begin{cases} \boldsymbol{\nabla}^2 V = 0, \qquad \boldsymbol{E}_0 = -\boldsymbol{\nabla}V, \\ k_m\boldsymbol{\nabla}^2 T + \frac{\sigma_m}{2}|\boldsymbol{E}_0|^2 = 0, \\ \mu_m\boldsymbol{\nabla}^2\boldsymbol{u} + \langle\boldsymbol{F}_{ET}\rangle = \boldsymbol{\nabla}P, \qquad \boldsymbol{\nabla} \cdot \boldsymbol{u} = 0, \end{cases} \tag{8}$$

where V is the electrical potential and the medium properties σ_m, μ_m and k_m are constants.

This system of equations can be solved sequentially since with the approximation of small temperature gradients, the electrical equation is not coupled with the thermal equation. Assuming the applied voltage has a peak to peak amplitude V_{pp}, the maximum temperature rise can be estimated by $\Delta T \sim \frac{\sigma_m V_{pp}^2}{8k_m}$, and the ACET fluid velocity is proportional to V_{pp}^4. In [1], Castellanos *et al* discuss the relative importance of buoyancy flows versus ac electrothermal flows [1]. The scaling of the buoyancy force is in V_{pp}^2 while the ACET force is in V_{pp}^4. At low voltages, buoyancy can be the dominant effect. Castellanos *et al* predict a transition between ACET and buoyancy around $L \approx 300\,\mu$m. They estimate that for $\sigma_m < 10^{-1}\,$S m^{-1}, a frequency of $f < 10^7\,$Hz, a characteristic length L less than $100\,\mu$m and an applied voltage greater than 1 V, buoyancy effects are lower than Brownian motion. Thus most papers presenting numerical simulations of the ACET flows driven by microelectrodes ($L \approx 25\,\mu$m) do not need to include buoyancy forces.

3. Enhanced model of ac electrothermal effect

We look into the validity of the standard model approximations in details.

The total temperature $T(t)$ solution of (4), for an applied ac electric field can be written as $T(t) = \langle T\rangle + T_\Delta(t)$ where $\langle T\rangle$ is the solution of the time-averaged equation and $T_\Delta(t)$ is the time dependent solution [1]. After time averaging and using the complex representation $\tilde{\boldsymbol{E}}$ of the electric field $\boldsymbol{E}$ with frequency ω, $\boldsymbol{E} = Re[\tilde{\boldsymbol{E}}e^{i\omega t}]$, (4) becomes

$$\boldsymbol{\nabla} \cdot (k_m\nabla\langle T\rangle) + \frac{\sigma_m}{2}|\tilde{\boldsymbol{E}}|^2 = 0. \tag{9}$$

The time-averaged temperature rise due to Joule heating can be estimated to be $\Delta T \approx \frac{\sigma_m V_{pp}^2}{8k_m} > 1\,^\circ$C for $V_{pp} = 10\,$V and $\sigma_m = 1\,$mS cm^{-1}. The typical thermal diffusion time can

be estimated by $\tau_{\text{diff}} = \frac{\rho_{\text{m}}c_p L^2}{k_m}$. For a characteristic length $L = 100\,\mu$m, τ_{diff} is of order of 0.1 s. The temperature deviation from the averaged temperature, $T_\Delta(t)$ can be approximated to be the solution of

$$\left| \frac{\partial T_\Delta}{\partial t} \right| \approx \frac{\sigma_{\text{m}}}{2\rho_{\text{m}}c_p}|E|^2,$$

and hence $|T_\Delta(t)| \approx \frac{\sigma_{\text{m}}}{4\omega\rho_{\text{m}}c_p}|\tilde{E}|^2. \quad (10)$

For an applied electric field with a frequency of 1 MHz, the relative importance of $T_\Delta(t)$ on the total temperature is $|\frac{T_\Delta}{T}| \approx \frac{1}{2\omega\tau_{\text{diff}}} \ll 1$. The temperature deviation, T_Δ is thus negligible in the temperature expression. However, the time derivative of T_Δ cannot be necessarily neglected likewise, since $|\frac{\partial T_\Delta}{\partial t}| \approx \frac{\sigma_{\text{m}}V_{\text{pp}}^2}{8\rho_{\text{m}}c_p L^2} \approx \frac{\Delta T}{\tau_{\text{diff}}} \gg 1$, for $V_{\text{pp}} = 10$ V and $\sigma_{\text{m}} = 1\,\text{mS cm}^{-1}$. Similarly,

The electrical equations (3) can be rewritten as

$$-(\sigma_{\text{m}}\boldsymbol{\nabla} \cdot \tilde{E} + \tilde{E} \cdot \boldsymbol{\nabla}\sigma_{\text{m}}) = \frac{\partial \rho_e}{\partial t} = \frac{\partial \varepsilon_{\text{m}}}{\partial t}\boldsymbol{\nabla} \cdot \tilde{E} + \varepsilon_{\text{m}}\boldsymbol{\nabla} \cdot \frac{\partial \tilde{E}}{\partial t}$$
$$+ \frac{\partial \tilde{E}}{\partial t} \cdot \boldsymbol{\nabla}\varepsilon_{\text{m}} + \tilde{E} \cdot \boldsymbol{\nabla}\frac{\partial \varepsilon_{\text{m}}}{\partial t}. \quad (11)$$

To understand the importance of each terms, we look at ratios of the terms in $\frac{\partial \varepsilon_{\text{m}}}{\partial t}$ on the right over the terms on the left:

$$\left| \frac{1}{\sigma_{\text{m}}}\frac{\partial \varepsilon_{\text{m}}}{\partial t} \right| = \left| \frac{1}{\varepsilon_{\text{m}}}\frac{\partial \varepsilon_{\text{m}}}{\partial T}\tau\frac{\partial T_\Delta}{\partial t} \right| \approx c_\varepsilon \Delta T \frac{\tau}{\tau_{\text{diff}}} \quad \text{and}$$

$$\left| \frac{1}{\boldsymbol{\nabla}\sigma_{\text{m}}}\boldsymbol{\nabla}\frac{\partial \varepsilon_{\text{m}}}{\partial t} \right| = \left| \frac{\tau}{\frac{1}{\sigma_{\text{m}}}\frac{\partial \sigma_{\text{m}}}{\partial T}\boldsymbol{\nabla}T}\frac{1}{\varepsilon_{\text{m}}}\frac{\partial \varepsilon_{\text{m}}}{\partial T}\boldsymbol{\nabla}\frac{\partial T_\Delta}{\partial t} \right| \approx \frac{c_\varepsilon}{c_\sigma}\frac{\tau}{\tau_{\text{diff}}}. \quad (12)$$

If $\frac{\tau}{\tau_{\text{diff}}} \ll 1$, then $\frac{\partial \varepsilon_{\text{m}}}{\partial t}\boldsymbol{\nabla} \cdot \tilde{E}$ is negligible compared to $\sigma_{\text{m}}\boldsymbol{\nabla} \cdot \tilde{E}$ and $\boldsymbol{\nabla}\frac{\partial \varepsilon_{\text{m}}}{\partial t} \cdot \tilde{E}$ is negligible compared to $\boldsymbol{\nabla}\sigma_{\text{m}} \cdot \tilde{E}$.

Since $\frac{\tau}{\tau_{\text{diff}}} \ll 1$, in our experiments, the temporal dependence of the temperature can be ignored in (11). We obtain the electrical equation:

$$\boldsymbol{\nabla} \cdot \tilde{E} = -\frac{\boldsymbol{\nabla}\sigma_{\text{m}} + \mathrm{i}\omega\boldsymbol{\nabla}\varepsilon_{\text{m}}}{\sigma_{\text{m}} + \mathrm{i}\omega\varepsilon_{\text{m}}} \cdot \tilde{E}. \quad (13)$$

The equation for the real, E_{R}, and imaginary, E_{I}, parts of $\tilde{E}$ are

$$\boldsymbol{\nabla} \cdot \begin{pmatrix} E_{\text{R}} \\ E_{\text{I}} \end{pmatrix} = \frac{-1}{1 + (\omega\tau)^2}\begin{pmatrix} a & -b \\ b & a \end{pmatrix}\begin{pmatrix} \boldsymbol{\nabla}T \cdot E_{\text{R}} \\ \boldsymbol{\nabla}T \cdot E_{\text{I}} \end{pmatrix} \quad (14)$$

where $a = (c_\sigma + (\omega\tau)^2 c_\varepsilon)$ and $b = \omega\tau(c_\varepsilon - c_\sigma)$.

Expression (14) can be further simplified at low or high frequencies.

If $\omega\tau \ll 1$ (which is the case for our experiments), (14) can be reduced to

$$\boldsymbol{\nabla} \cdot \begin{pmatrix} E_{\text{R}} \\ E_{\text{I}} \end{pmatrix} = -c_\sigma\begin{pmatrix} \boldsymbol{\nabla}T \cdot E_{\text{R}} \\ \boldsymbol{\nabla}T \cdot E_{\text{I}} \end{pmatrix}. \quad (15)$$

If $\omega\tau \gg 1$, (13) can be reduced to

$$\boldsymbol{\nabla} \cdot \begin{pmatrix} E_{\text{R}} \\ E_{\text{I}} \end{pmatrix} = -c_\varepsilon\begin{pmatrix} \boldsymbol{\nabla}T \cdot E_{\text{R}} \\ \boldsymbol{\nabla}T \cdot E_{\text{I}} \end{pmatrix}. \quad (16)$$

In both cases, if no electrical boundary condition written in complex notations introduces an imaginary part, then $E_{\text{I}} = 0$. The boundary condition representing the ac applied voltage on the electrodes can be expressed using the complex representation, $\tilde{V}$, with $V = Re[\tilde{V}e^{\mathrm{i}\omega t}]$ where $\tilde{V}$ can have a real and imaginary part. For most AC electrothermal devices, there is either no time phase shift between electrodes or a $\pi/2$ time phase shift between electrodes and consequently $\text{Im}[\tilde{V}] = 0$.

In terms of electrical potential ($\tilde{E} = -\boldsymbol{\nabla}\tilde{V}$), the electrical equation becomes

$$\nabla^2\tilde{V} = \gamma \cdot \boldsymbol{\nabla}\tilde{V}, \quad (17)$$

where $\gamma = -c_\sigma\boldsymbol{\nabla}T$, if $\omega\tau \ll 1$, (and $\gamma = -c_\varepsilon\boldsymbol{\nabla}T$, if $\omega\tau \gg 1$). The electrical potential is a solution of a convection-diffusion equation with convection vector γ and diffusion coefficient $D = 1$. The Peclet number for this equation is given by $Pe_{\text{ET}} = c_\sigma\Delta T$ if $\omega\tau \ll 1$ (and $Pe_{\text{ET}} = c_\varepsilon\Delta T$ if $\omega\tau \gg 1$). For a temperature elevation $\Delta T > 10\,^\circ$C and $\omega\tau \ll 1$, the voltage deflection by the gamma field, γ, becomes non negligible as $Pe_{\text{ET}} > 0.2$. Indeed, the 'small temperature gradient' approximation of (6) is actually a small temperature elevation approximation and is valid only if $Pe_{\text{ET}} \ll 1$.

At high temperature in the fluid, the temperature dependences of the fluid properties cannot be neglected either. Aqueous solution dynamic viscosity, μ_{m}, is highly dependent on temperature which can be described by a polynomial equation [8]. Aqueous solution conductivity is inversely proportional to the dynamic viscosity. For a temperature rise of $10\,^\circ$C, dynamic viscosity decreases, and the electrical conductivity increases by about 20%. Thus their temperature dependence is not negligible. Aqueous solution thermal conductivity, k_{m}, only changes by 2% for a temperature increase of $10\,^\circ$C. Hence it can be assumed to be constant.

We hence model the ac electrothermal flows, assuming $\omega\tau \ll 1$, using the following set of equations:

$$\begin{cases} \nabla^2\tilde{V} = c_\sigma\boldsymbol{\nabla}T \cdot \boldsymbol{\nabla}\tilde{V}, & \tilde{E} = -\boldsymbol{\nabla}\tilde{V}, \\ \boldsymbol{\nabla} \cdot (k_{\text{m}}\boldsymbol{\nabla}T) + \frac{\sigma_{\text{m}}(T)}{2}|\tilde{E}|^2 = 0, \\ \boldsymbol{\nabla} \cdot (\mu_{\text{m}}(T)(\boldsymbol{\nabla}u + (\boldsymbol{\nabla}u)^{\text{T}})) + F = \boldsymbol{\nabla}P, \ \boldsymbol{\nabla} \cdot u = 0 \end{cases} \quad (18)$$

and the boundary conditions presented in figures 1(*c*) and (*d*) The force F can be either expressed as the ETH Force only $F = \langle F_{\text{ET}} \rangle$ (enhanced model) or as the sum of ETH force and the buoyancy force: $F = \langle F_{\text{ET}} \rangle + F_{\text{b}}$ (full enhanced model).

The time-averaged electrostactic body force is here given by

$$\langle F_{\text{ET}} \rangle = \frac{\varepsilon_{\text{m}}(T_0)}{2}\left[(c_\varepsilon - c_\sigma)(\boldsymbol{\nabla}T \cdot \tilde{E})\tilde{E} - \frac{1}{2}c_\varepsilon\boldsymbol{\nabla}T|\tilde{E}|^2 \right]. \quad (19)$$

4. Experimental setup

Experiments are performed in a $250\,\mu$m deep PDMS well. The ac electric field is generated between three $35\,\mu$m thick gold electrodes (figure 1). Each electrode is deposited above 1.1 mm thick PCB board (FR4). The separation between
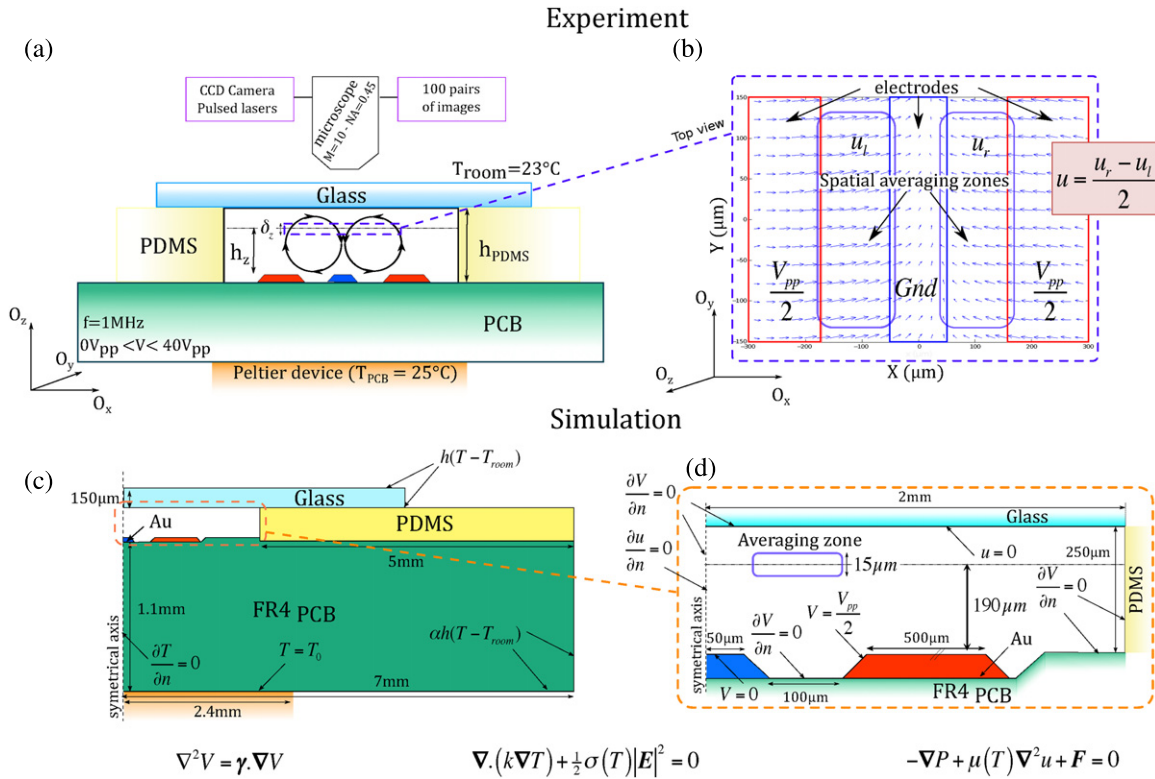
Figure 1. (*a*) Side view of the experimental set-up: flow velocities are measured in the horizontal plan at a height h_z above the electrodes. (*b*) Top view of the velocity flow in the horizontal plane. The plotted velocity **u** is spatially averaged above the two gaps. (*c*) Side view of half of the device with the thermal limit boundaries. (*d*) Zoom of half of the microfluidic room with the fluid and electric limit boundaries.

electrode is $100\,\mu$m. The central $150\,\mu$m wide electrode is grounded, while a sinusoidal voltage of 1 MHz with amplitude ranging from 0 to $40V_{pp}$ (peak to peak) is applied to the side electrodes. High frequency signal is chosen to limit low frequency effects (e.g. electrolysis, ac electro-osmosis). The microfluidic chamber is covered by a $150\,\mu$m thick glass cover slip. The room temperature is set slightly below $T_{room} = 23\,°$C. To homogenize the temperature in the horizontal plane and to provide a reference temperature for the model, the temperature under the PCB board is set at $T_{PCB} = 25\,°$C via a thermoelectric device thereby keeping a temperature difference ($\Delta T_0 = T_{PCB} - T_{room} \approx 2\,°$C) small enough to avoid natural convection when no current is applied

In this set-up the Joule heating creates a hot spot above the center electrode and the interaction of the gradient of permittivity and conductivity with the electric field generates vortices. Flows ranging from 10 to $500\,\mu$m s^{-1} are measured by μPIV [9] using a microscope Eclispe TE600 (Nikon, Melville, NY, US) and two pulsed lasers MiniLase II-30 (New Wave research, Fremont, CA, US) synchronized with a camera PIVCAM 13.8 (TSI, Shoreview, MN, US). The velocities of $1\,\mu$m latex beads are extracted at $h_z = 190$ or $250\,\mu$m above the electrodes using a custom PIV interrogation software [10].

The particle images are taken using an infinity-corrected objective lens (Nikon, $M = 20$, $NA = 0.45$). A relay lens with magnification $0.5\times$ was used to reduce the system magnification to $M = 10$, thereby providing a larger field of view. The depth of the PIV measurement is estimated to be $\delta_z = \pm 7.5\,\mu$m [11].

The relatively large, $d_p = 1\,\mu$m, diameter particles were chosen to dampen Brownian motion without exhibiting significant DEP forces. The CCD camera pixel size is $d_{pix} = 6.7\,\mu$m. Accounting for geometric, diffraction and small variations from the object plane [12], the particle-image diameter is estimated to be $d_e \approx 17.5$–$65\,\mu$m. This results in a ratio of $\frac{d_e}{d_{pix}} = 2.5$–$9.3$. Following Prasad *et al* [13], for $\frac{d_e}{d_{pix}} > 3$–4, the uncertainly in locating the peak is approximately 1/10th of the particle-image diameter [14]. When projecting back into the flow, the measurement uncertainty is $\delta_x \approx \frac{d_e}{10M}$, which corresponds to $\delta_x \approx \frac{3.8}{100} = 38$ nm.

The particle density was chosen such that there was a sufficient number of particle images in an interrogation window, without creating a very large background noise due to out-of-focus particle images. In the current experiments, we have approximately $N_p = 2$ particles for each 64×64 pixel interrogation windows. At low voltage conditions, $N_{ens} = 100$ correlation functions were ensemble averaged for each interrogation region. The resulting correlation functions were fitted with Gaussian functions to determine the particle-image displacement peaks. This interrogation strategy significantly reduces pixel-locking bias and provides highly reliable velocity data.

Because of the electrode configuration, the flow is 2D, symmetric and perpendicular to the electrodes. The velocity vectors is thus averaged over $N_s = 50$ independent velocity vectors above each gap (figure 1(*c*)). Perturbation flows are removed by subtracting the offset velocity field at zero.

The uncertainty in velocity primarily results from unbiased errors due to uncertainty in peak location and random
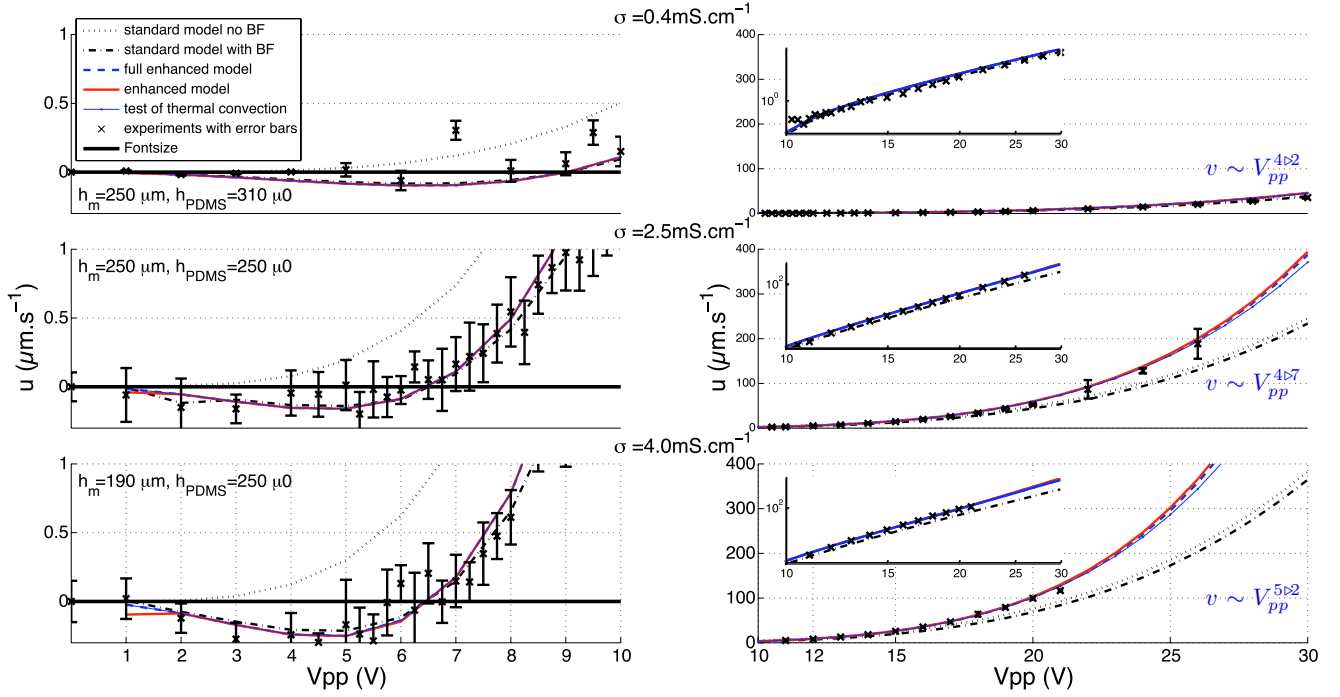
Figure 2. Plot of the fluid velocities for conductivities $\sigma_m = 0.4,\ 2.5,\ 4.0\,\text{mS cm}^{-1}$ according to the applied voltage V_{pp}. Experimental measurement (black cross), standard model (8) without buoyancy force (black dotted line), standard model with buoyancy force (black dotted–dashed line), enhanced model (red line), full enhanced model (blue dashed line), full enhanced model with thermal convection (thin blue line with dots). A positive velocity corresponds to vortices flowing down above the central electrode whereas the negative velocities corresponds to vortices flowing up above the central electrode. (*a*) shows the velocities at low voltages on a linear scale. (*b*) shows the velocities at high voltages on a linear scale and a log–log scale.

walk of the particles due to Brownian motion [14]. Accounting for ensemble correlation and spatial averaging, yields,

$$\delta_{uB} = \sqrt{\frac{2D}{2\Delta t\,N_{ens}N_s}} \approx 30\,\text{nm s}^{-1}, \qquad (20)$$

$$\delta_{uPD} = \frac{0.1 d_e}{M\,\Delta t\,\sqrt{2N_{ens}N_s}} \approx 40\,\text{nm s}^{-1}. \qquad (21)$$

These two errors are statistically independent and contribute to the total unbiased error: $\delta = \sqrt{\delta_{uPD}^2 + \delta_{uB}^2} \approx 50\,\text{nm s}^{-1}$. The error is smaller than the root mean square (rms) measured error (see errorbars in the figure 2) due to the finite distribution of the actual flow.

5. Numerical simulations

Numerical simulations are performed using the commercial finite element software Comsol Multiphysics v4.2a (COMSOL Inc., Stockholm, Se) in a 2D model including PCB board, electrodes, PDMS chamber and cover slip as described in figures 1(*c*) and (*d*). Comparing the 2D thermal model to a 3D model of the full device, PCB heat conductivity k_{PCB} and the heat transfer coefficient h_{PCB} have been increased by a shape factor of 7 so as to take into account 3D heat dissipation.

The 2D domain is meshed using a fine triangular mesh of over 13 000 elements with a growth ratio of 1.3. The highest gradient of the electrical, thermal and fluid solutions appears in the liquid chamber and in the electrodes for $|x| < 500\,\text{nm s}^{-1}$.

The maximum element size used in this region is $7\,\mu\text{m}$. Elsewhere the maximum element size is 1 mm. A much coarser grid is needed to observe a grid dependence.

The three equations, (18), were first solved sequentially without coupling and with fixed coefficient (standard model solution). This solution was then used as initial condition for our enhanced model. The accuracy constraint was set by using a 10^{-3} relative error.

To be compared with experiments, the velocities obtained from simulation are averaged in a 2D region above each gap, $(x, z) \in [50\,\mu\text{m};\,150\,\mu\text{m}] \times [h_z - 7.5\,\mu\text{m};\,h_z + 7.5\,\mu\text{m}]$. The results are shown in figure 2 for conductivities $\sigma_m = 0.4,\ 2.5,\ 4.0\,\text{mS cm}^{-1}$. Following the velocity measure described in figures 1(*a*) and (*b*), a positive velocity **u** corresponds to vortices flowing down above the central electrode (i.e. ACET). Conversely, a negative velocity corresponds to vortices flowing up above the central electrode (i.e. buoyancy).

The standard model was simulated with and without buoyancy. The enhanced model was simulated with buoyancy force using the temperature dependent function for the electrical conductivity, $\sigma_m(T)$, and the dynamic viscosity $\mu_m(T)$ with no thermoelectric coupling ($\gamma = 0$) (enhanced model). Then it was solved with the correct expression for the γ field (full enhanced model). The measured velocities at high voltage, for $\sigma_m = 2.5,\ 4.0\,\text{mS cm}^{-1}$, have amplitudes above $100\,\mu\text{m s}^{-1}$ leading to a $Pe_T > 0.5$. We tested the effect of thermal convection on our enhanced model (thin blue line with dots). The error introduced by neglecting the convection

term in our case is negligible compared with the error resulting by the use of the standard model at high voltage and high conductivities.

6. Results and discussion

The magnitude of the velocity is plotted against V_{pp} in figure 2. Experimental measurements for conductivities $\sigma_m = 0.4, 2.5, 4.0 \, \text{mS cm}^{-1}$ are plotted as black crosses. The measurements at high applied voltages are fitted to a V_{pp}^k curve. For the low conductivity experiments, $k \approx 4$ but at higher conductivities where Joule heating is more significant, k tends to 5. This shows a discrepancy between the standard model (8) that predicts scaling of velocity as V_{pp}^4 and the fluid velocity measured. At high conductivity, and high voltage, the Joule heating in the fluid is significant, which leads to a deviation of the observed ac electrothermal fluid flow from that predicted by the small temperature gradient approximation. Moreover, we also observe that for low applied voltage, the vortices rotate in the opposite direction as ACET flows (i.e. flowing up above the central electrode) and have a dependence in V_{pp}^2.

According to figure 2, our experimental measures (black cross) of the fluid velocities for all three conductivities fit the numerical solution of our full enhanced model, (18), with the buoyancy effect for the full range of applied voltages. The standard model, (8), underpredicts velocities at high voltage. Slight differences occur at low voltages, which can be explained by the uncertainties due to the unbiased error in the μPIV measurements (20), (21).

At low voltages, our μPIV measurement processing permits to extract small velocities out of the Brownian motion. The measured low negative velocities are explained by adding the buoyancy effect to the model. The amplitude of the velocity increases following a V_{pp}^2 law till a critical voltage at which the direction of the vortices change. As expected, the standard model with buoyancy force fit at low voltages. The ratio of ACET force over buoyancy can be approximated by

$$\frac{F_{ET}}{F_b} \approx \frac{\varepsilon_m |c_\varepsilon - c_\sigma| V_{pp}^2}{8 \rho_m \beta g L^3}. \tag{22}$$

At low voltage and mesoscale, the competition between ACET and buoyancy effects is apparent. The critical voltages at which ACET flows start dominating over buoyancy are almost identical for all conductivities, thereby confirming that the ratio of ACET force over buoyancy force (22) does not depend on conductivity. The slight shift occurring at $0.25 \, \text{mS cm}^{-1}$ compared with the two other plots is explained by the difference of PDMS height in the experiment for this conductivity. However, at smaller scale, the critical voltage will quickly decrease since the ratio of ACET over buoyancy depends on L^{-3}.

The strong thermoelectric coupling and the temperature dependence expression of parameters μ_m and σ_m explain the fluid velocity dependence in V_{pp}^k with $k > 4$ for high conductivity solutions at high voltages. The electrical conductivity increases by 20% for a temperature rise of $10 \,^\circ\text{C}$ which will rise the temperature in the fluid by the same amount.

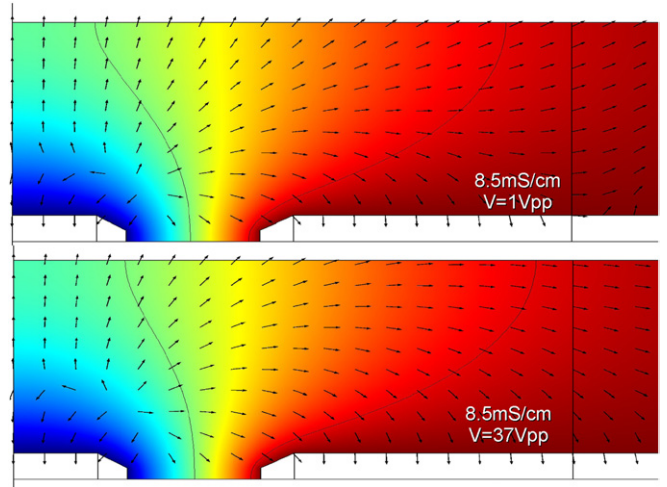**Figure 3.** Contour plots of the electrical potential V and normalized arrow surface of the gamma field, γ, in the fluid for low voltage $1 \, V_{pp}$ and high voltage $37 \, V_{pp}$ at high conductivity $8.5 \, \text{mS cm}^{-1}$. For high temperature gradient, isopotential lines are advected away from the center electrodes.

The dynamic viscosity decreases by 20% for a temperature rise of $10 \,^\circ\text{C}$ which will additionally rise the velocity.

The thermoelectric coupling changes the electrical potential distribution according to the convection-diffusion equation (17). Two contour plots of the electrical potential superimposed with normalized arrow surface of the gamma field, γ, are presented for $\sigma_m = 8.5 \, \text{mS cm}^{-1}$ and two different peak-to-peak voltages $1 V_{pp}$ and $37 V_{pp}$ (figure 3). At high voltage, the electrical potential contours move along the gamma field away from the center electrode according to (17). This deflection can be understood as the advection of the isopotential lines which occurs at high temperature where the electrothermal Peclet number Pe_{ET} is not negligible.

In our case, the variability of the conductivity and viscosity has more influence to the change in power-law exponent than the potential advection. With our mesoscale device ($L \approx 100\text{–}200 \, \mu\text{m}$), higher voltage is required to obtain significant flows ($V_{pp} > 10V$, figure 2). Consequently electrolysis usually occurs before any significant potential advection. However, as high temperature is reached mainly because of high voltages and weak thermal conductivity of the PCB board, the temperature dependence of conductivity and viscosity are significant. Conversely, for smaller devices such as microelectrodes deposited on silicon wafer, ($L \approx 10\text{–}20 \, \mu\text{m}$), gradients may increase up to a factor of 10. In that case, small spatial changes to the electrical potential have a high impact on the calculations of the gradients, requiring to take into account the advection of the potential. However, the temperature rise may not be as significant since lower voltages are required and the temperature is more easily dissipated.

Our approach of the ACET modelling successively shows how the standard ACET model (8) is affected by high Joule heating (corresponding to high conductivities and high voltages). The full enhanced model presented here using a electrical thermal coupling and temperature dependent expression for the electrical conductivity and dynamic viscosity should be used for a general temperature rise

J. Phys. D: Appl. Phys. **45** (2012) 185301

S Loire *et al*

above $\approx 5\,^{\circ}$C. Furthermore, the importance of the competition between ACET and buoyancy driven convective flow at low voltages was observed experimentally and theoretically.

Acknowledgments

References

[1] Castellanos A, Ramos A, González A, Green N G and Morgan H 2003 Electrohydrodynamics and dielectrophoresis in microsystems: scaling laws *J. Phys. D: Appl. Phys.* **36** 2584

[2] Gonzáles A, Ramos A, Morgan H, Green N G and Castellanos A 2006 Electrothermal flows generated by alternating and rotating electric fields in microsystems *J. Fluid Mech.* **564** 415–33

[3] Sigurdson M, Wang D and Meinhart C D 2005 Electrothermal stirring for heterogeneous immunoassays *Lab Chip* **5** 1366–73

[4] Sigurdson M, Chang D E, Tuval I, Mezić I and Meinhart C D 2007 Ac electrokinetic stirring and focusing of nanoparticles *BioMEMS and Biomedical Nanotechnology* ed M Ferrari *et al* (New York: Springer) pp 243–55

[5] Ramos A, Morgan H, Green N G and Castellanos A 1998 Ac electrokinetics: A review of forces in microelectrodes *J. Phys. D: Appl. Phys.* **31** 2338–53

[6] Sin M L Y, Gau V, Liao J C and Wong P K 2010 Electrothermal fluid manipulation of high-conductivity samples for laboratory automation applications *J. Assoc. Laboratory Automation* **15** 426–32

[7] Melcher J R 1981 *Continuum Electromechanics* (Cambridge, MA: MIT Press)

[8] Lide D R 2000 *Handbook of Chemistry and Physics* 81 edn (New York: CRC Press)

[9] Santiago J G, Wereley S T, Meinhart C D, Beebe D J and Adrian R J 1998 A particle image velocimetry system for microfluidics *Exp. Fluids* **25** 316–19

[10] Meinhart C D, Wereley S T and Santiago J G 2000 A PIV algorithm for estimating time-averaged velocity fields *J. Fluid Eng.* **122** 285–9

[11] Meinhart C D, Wereley S T and Gray M H B 2000 Volume illumination for two-dimensional particle image velocimetry *Meas. Sci. Technol.* **11** 809–14

[12] Olsen M G and Adrian R J 2000 Out-of-focus effects on particle image visibility and correlation in microscopic particle image velocimetry *Exp. Fluids* **29** S166–74

[13] Prasad A, Adrian R, Landreth C and Offutt P 1992 Effect of resolution on the speed and accuracy of particle image velocimetry interrogation *Exp. Fluids* **13** 105–16

[14] Meinhart C D, Wereley S T and Santiago J G 1999 PIV measurements of a microchannel flow *Exp. Fluids* **27** 414–9